Improved Snow Property Retrievals by Solving for Topography in the Inversion of At-sensor Radiance Measurements

Brenton A. Wilder[1], Joachim Meyer[1], Josh Enterkine[1], Nancy F. Glenn[1*]

[1]Department of Geosciences, Boise State University, Boise, ID, USA

Correspondence to: Nancy F. Glenn (nancyglenn@boisestate.edu)

Abstract

Accurately modelling optical snow properties like snow albedo and specific surface area (SSA) are essential for monitoring the cryosphere in a changing climate and are parameters that inform hydrologic and climate models. These snow surface properties can be modelled from spaceborne imaging spectroscopy measurements but rely on Digital Elevation Models (DEMs) of relatively coarse spatial scales (e.g. Copernicus at 30 m), which degrade accuracy due to errors in derived products – ~~like~~ such as slope and aspect. In addition, snow deposition and redistribution can change the apparent topography and thereby static DEMs may not be considered coincident with the imaging spectroscopy dataset. Testing in three different snow climates (tundra, maritime, alpine), we established a new method that

simultaneously solves snow, atmospheric, and terrain parameters, enabling a solution that is more unified across sensors and introduces fewer sources of uncertainty. We leveraged imaging spectroscopy data from AVIRIS-NG and PRISMA (collected within 1 hour) to validate this method and showed a 25% increase in performance for the radiance-based method ~~versus using~~over the static method when estimating SSA. This concept can be implemented in ~~future~~ missions such as Surface Biology and Geology (SBG), Environmental Mapping and Analysis Program (EnMap), and Copernicus Hyperspectral Imaging Mission for the Environment (CHIME).

Key Words: Imaging Spectroscopy, Snow Properties, Topography, Snow Albedo

1 Introduction

Accurately mapping snow surface properties is essential for seasonal snow zones in a changing climate especially in regions where seasonal snowpack is expected to change dramatically in the coming decades (Siirila-Woodburn et al., 2021). For example, snow albedo plays a crucial role in melting of the snowpack during the ablation season (Wang et al., 2020) with changes in snow albedo directly affecting the amount of absorbed solar radiation, and therefore the amount of snow that is melted off~~ as liquid water~~. Throughout the winter season, snow albedo fluctuates due in part to grain size (Seidel et al., 2016) and light absorbing particles (Kaspari et al., 2015; McKenzie, 2020; Schmale et al., 2017; Skiles & Painter, 2017). With a limited number of *in situ* snow stations around the globe ~~measuring surface properties~~, and the snow surface~~s~~ constantly undergoing metamorphism across space and time, satellite imagery represents the best potential for spatially and temporally complete mapping of snow properties. Accurately retrieving snow albedo and other snow surface properties from satellite imagery is paramount, especially in a rapidly changing climate (Malmros et al., 2018).

Retrieval of snow properties from satellite remote sensing relies on Digital Elevation Models (DEMs) to correct for local terrain effects (Bair et al., 2021; Bair et al., 2022; Dozier et al., 2022). In a previous study, researchers found global DEM products to have "blunders and errors" when compared to airborne lidar, particularly in derived slope and aspect which cause severe errors in calculated cosine of local solar illumination angles (μ_s) (Dozier et al., 2022). ~~Dozier et al. (2022)~~They found errors in μ_s ~~local solar illumination angles~~ ranging from 0.048 to 0.117 (dimensionless) across several sites for Copernicus global DEMs caused by errors in slope and aspect. The ~~cosine of the local solar illumination angle,~~ μ_s~~,~~ term is a function (Eq. 1) of slope angle (S), ~~slope aspect~~slope azimuth angle or aspect (A), solar zenith angle (θ_0), and solar azimuth angle (ϕ_0) – with the last two being well constrained:

$$\mu_s = \max[0,\ \cos(\theta_0)\cos(S) + \sin(\theta_0)\sin(S)\cos(\phi_0 - A)] \qquad (1)$$

Because θ_0 and ϕ_0 are calculable with low errors ~~(less than 0.05°)~~, the biggest contribution to errors in μ_s stem from slope and aspect. Errors in μ_s increase monotonically with increasing θ_0 (e.g., sun setting has high θ_0, as does solar noon in high latitude winters). This phenomenon can be explained by plotting Eq. 1 for various ~~solar zenith angles,~~ θ_0 ~~,~~ (Figure 1). Put simply, at higher θ_0 there is a higher standard deviation in μ_s surrounding a known slope and aspect (with some temporally consistent uncertainty), increasing the probability and magnitude of such an error. If one were to compute standard deviations of μ_s across varying θ_0, one would arrive at similar errors of μ_s presented in Dozier et al. (2022). For clarity, in Figure 1 we have highlighted an example case with slope=25° +/- 4.73 and aspect=280° +/- 36.3. Example uncertainties for this exercise can be found in Table 2 of Dozier et al. (2022). ~~For example, if one were to arbitrarily choose slope and aspect (with some uncertainty), and varying θ_0 (20-70°), one could find a similar range of errors as presented in Dozier et al. (2022).~~

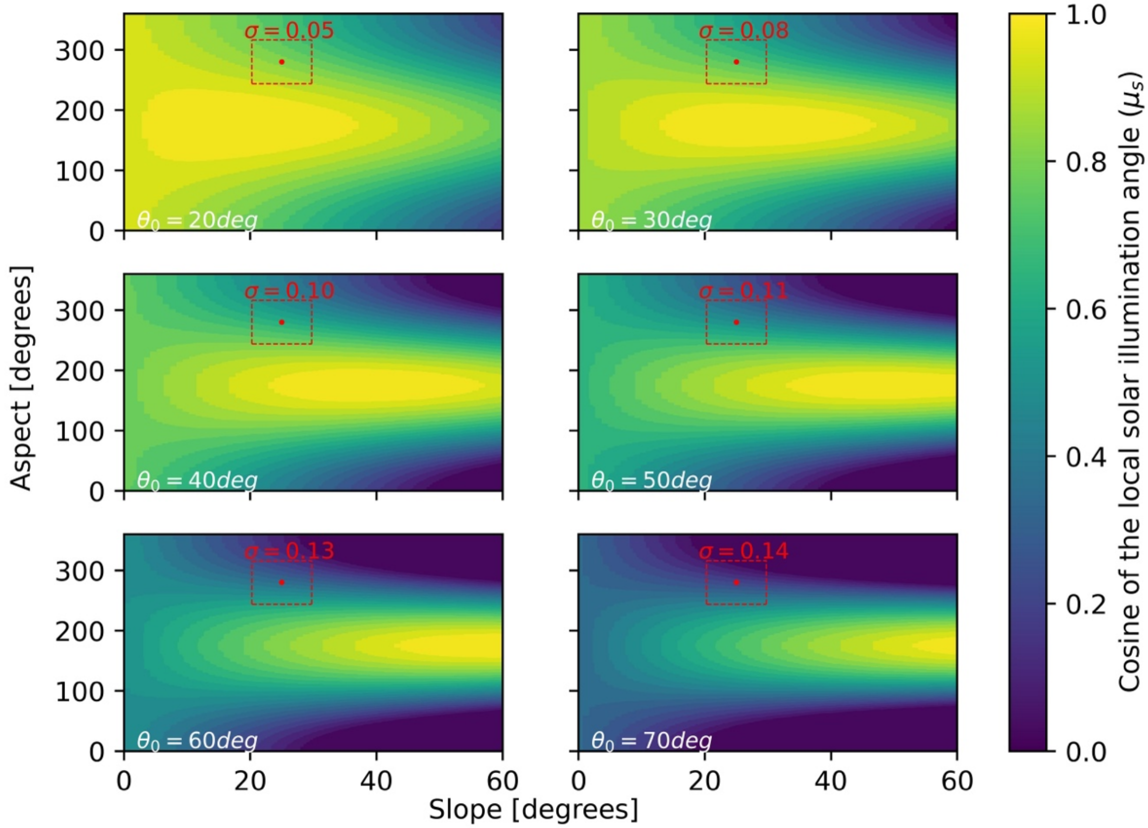

Figure 1. Cosine of local illumination angles (μ_s) as a function of slope (x-axis) and aspect (y-axis) incremented by 1°, ~~.~~ illustrating the problem at higher latitude, and/or winter acquisitions, where standard deviation (σ) of μ_s increases monotonically with solar zenith angles (θ_0). Aspect is shown here measured clockwise from north (with north containing a discontinuity at 360 degrees). ~~Increasing solar zenith angles (θ_0) illustrates the problem at higher latitude, and/or winter acquisitions, where variability increases with respect to slope and aspect.~~ For this illustration ϕ_0 is fixed at a value of 175°. The red dots represent the

example point at slope=25° +/- 4.73 and aspect=280° +/- 36.3 and are bordered by their uncertainty and the resulting σ.

Recent work has shown μ_s can be modelled using an optimal estimation framework given the Top of Atmosphere (TOA) radiance observed from imaging spectroscopy (Carmon et al., 2023). The authors solve for surface, atmospheric, and topographic state variables simultaneously in their model. This works physically because the partition of direct to diffuse light introduces a shape and magnitude effect on the TOA radiance spectra. However, retrieving snow optical properties is sensitive to directional reflectance which is significantly influenced by the viewing geometry ~~-~~and surface roughness (Bair et al., 2022), leading to possible shortcomings in this method specifically for snow covered pixels. To address this and expand upon this framework, we present a new method to account for terrain in snow covered areas. Our method was tested on pixels with greater than 75% snow cover in three different snow climates (tundra, maritime, and alpine) with spaceborne imaging spectroscopy with the aim to reduce error in derived snow properties by optimally solving for topography. The spaceborne results are validated against high confidence airborne spectrometer data ~~and further evaluated with error distributions~~. This work directly contributes to snow property retrievals in steep terrain and/or at times of high solar ~~illumination~~ zenith angles for

~~upcoming~~ satellite ~~imagine~~imaging spectroscopy missions such as Surface Biology and Geology (SBG) (Cawse-Nicholson et al., 2021), ~~and~~ Copernicus Hyperspectral Imaging Mission for the Environment (CHIME) (Celesti et al., 2022), and EnMap (Guanter et al., 2015).

2 Methods

2.1 Study area

For our study, we used *PRecursore IperSpettrale della Missione Applicativa* (PRISMA) imagery over three sites capturing different snow climates and solar zenith angles: San Juan Mountains (Colorado, USA, 29 April 2021, θ_0=27°), Mount Shasta (California, USA, 28 February 2021, θ_0=52°), and the Toolik area (Alaska, USA, 21 March 2021, θ_0=68°) (Figure 2). The San Juan Mountains location is considered a high alpine site located in interior continental USA with an elevation range of 2208-4129 m. The Mount Shasta site is a maritime snow climate along the western coast of USA with an elevation range of 750-4232 m. The Toolik site (elevation range = 504-1748 m) is a high-latitude tundra site, being mostly flat but with steep sections along the Brooks Range (along the southern part of the image). PRISMA, launched by the Italian Space Agency (ASI) and beginning operation on March 22, 2019, is a spaceborne imaging spectroscopy mission collecting radiance at 30 m spatial resolution across 239~~7~~ bands spanning 400-2500 nm at a spectral resolution better than 12 nm across ~~at a spectral resolution of 9.24 nm and 9.27 nm in~~ the visible-near and shortwave infrared~~, respectively~~ (Cogliati et al., 2021).

To validate our method, we used four existing Airborne Visible Infrared Imaging Spectrometer-Next Generation (AVIRIS-NG) flightlines over the San Juan Mountains from 29 April 2021 (flying 1 hour after PRISMA acquisition). AVIRIS-NG collects radiance measurements at variable spatial resolution (depending on the flight altitude) across 425 bands spanning 380-2510 nm in 5nm intervals (Green et al., 2023). For this flight, data were collected at 4 m spatial resolution. We downloaded AVIRIS-NG apparent reflectance from National Snow and Ice Data Center (NSIDC) and observation geometry data from NASA Search Earth Data (Skiles & Vuyovich, 2023).

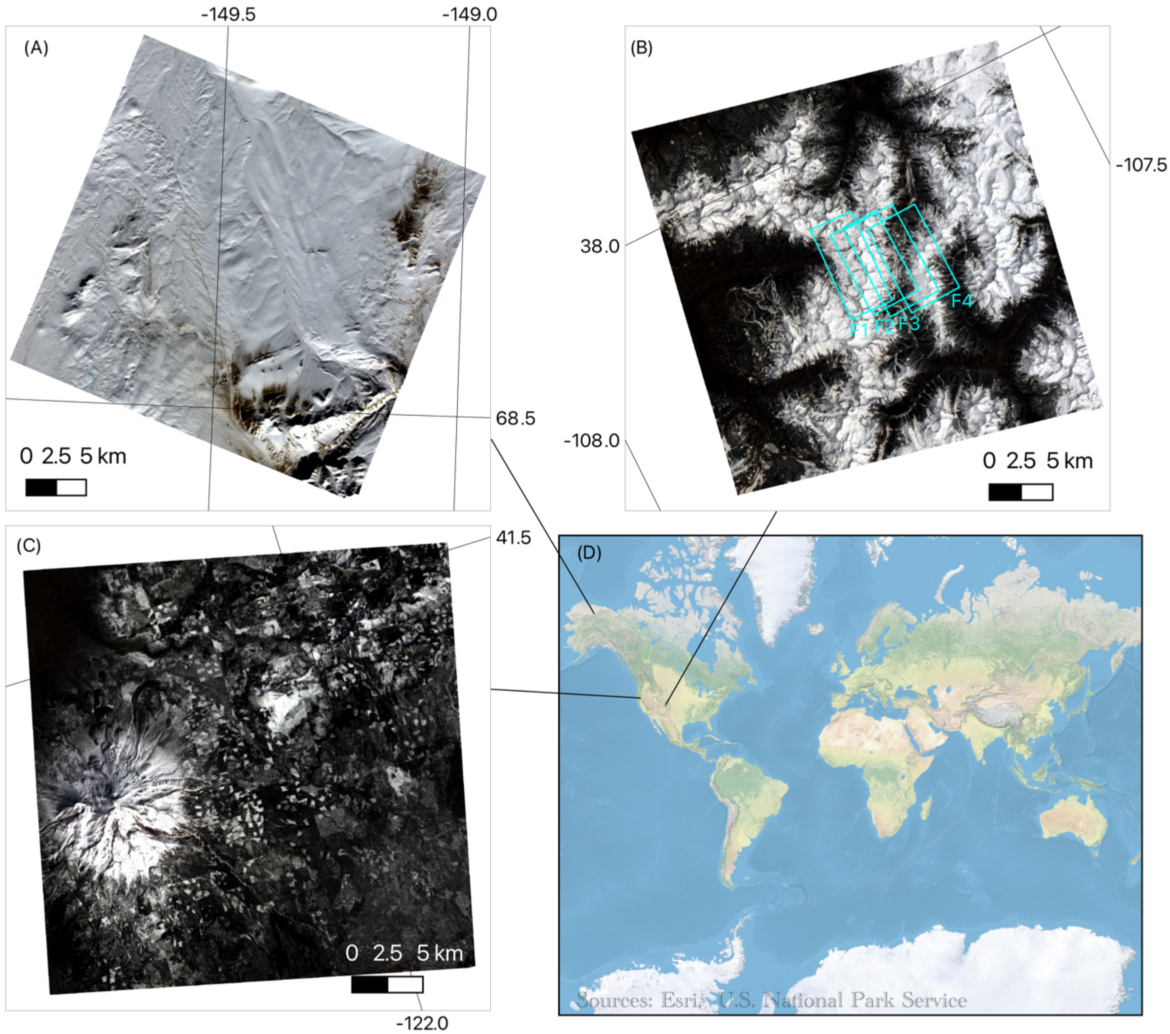

Figure 2. PRISMA true colour images for Toolik on 21 March 2021 (A), San Juan Mountains on 29 April 2021 (B), and Mount Shasta on 28 February 2021 (C). Four coincident AVIRIS-NG flightlines (F1-F4) are shown in cyan over the San Juan Mountains.

2.2 Modelling surface, atmosphere, and topography from PRISMA

The algorithmic improvements build off a workflow that estimates snow properties given PRISMA TOA radiance, titled Global Optical Snow properties via High-speed Algorithm using K-means (GOSHAWK) (~~Wilder et al., 2023;~~ Wilder et al., 2024). In short, ~~GOSHAWK~~ our method uses the analytic asymptotic radiative transfer model (AART) (Kokhanovsky & Zege, 2004) coupled with libRadtran (Mayer & Kylling, 2005) to invert snow surface and atmospheric properties (Bohn et al., 2021; Dalcin & Fang, 2021), and fractional covers of mixed pixels under varied lighting conditions using non-linear numerical optimization (Bair et al., 2021). The parameters solved for in the optimization routine include fractional covers, specific surface area (SSA), light absorbing particle concentration (modelled as ~~soot~~dust), liquid water ~~content (LWC)~~ percentage, dimensionless aerosol optical depth at 550nm, and columnar water vapor in the atmosphere. Here, we expand upon the ~~GOSHAWK~~ algorithm considering recent work showing the capacity to estimate μ_s from TOA radiance (Carmon et al., 2023; Bohn et al. 2024). This ~~capacity~~ idea is demonstrated in Figure 3 using fixed snow properties via AART and fixed atmosphere properties via libRadtran across the range of plausible μ_s (i.e. 0 to 1). Like the findings in Carmon et al. (2023), Figure 3 shows that μ_s controls both the spectral shape and magnitude of observed TOA radiance with the effect varying across wavelengths. The greatest shape effect can be seen in the visible spectrum (roughly 400-700 nm) due to the magnitude of the diffuse irradiance. In combination with the magnitude and shape shift, this parameter becomes solvable during optimization due to its strong separability – especially when considering the entire spectrum data from a hyperspectral remote sensing source such as PRISMA. It is important to note that μ_s impacts both the AART estimation of snow reflectance and libRadtran estimation of incoming solar irradiance.

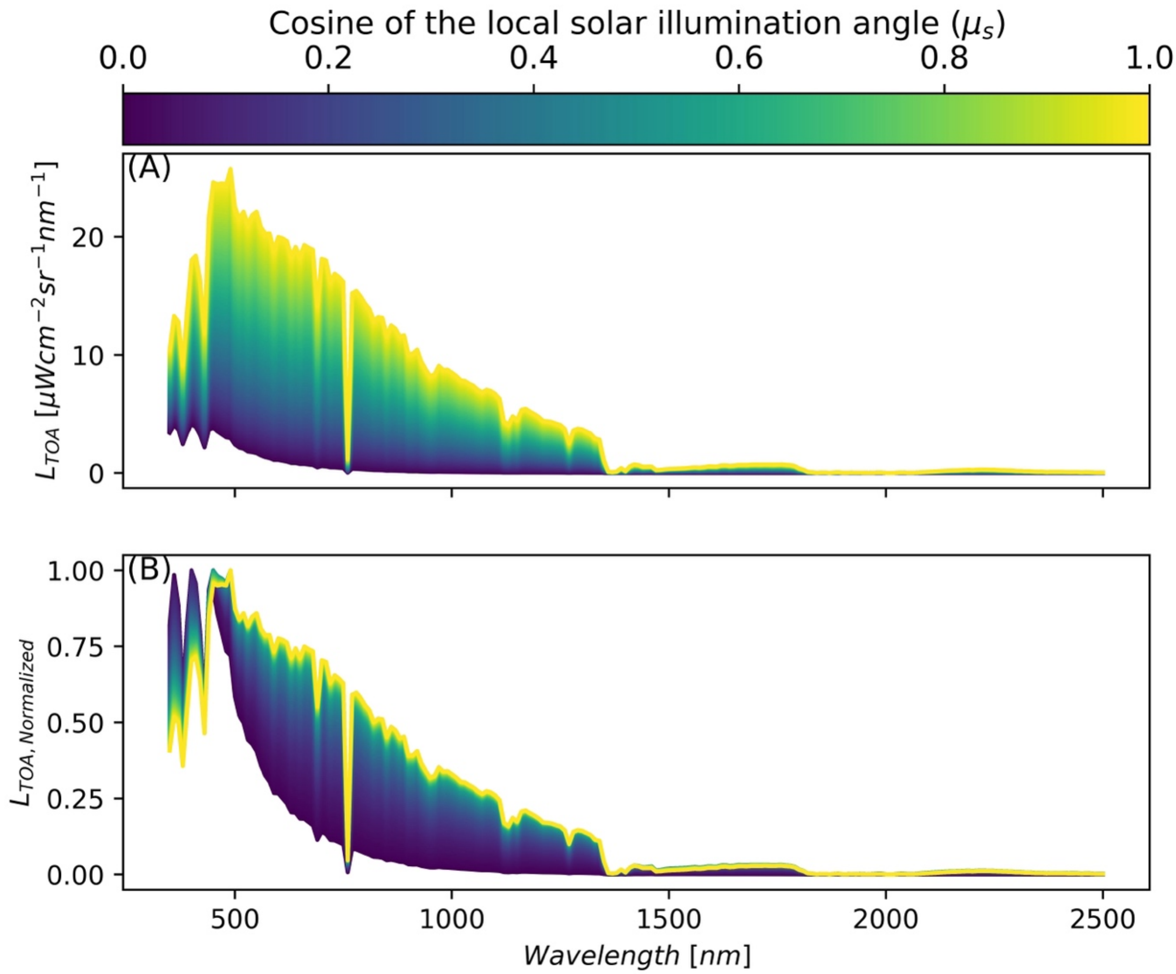

Figure 3. Synthetic data showing change in magnitude (A) and shape (B) of top of atmosphere radiance (L_{TOA}) with respect to changing local solar illumination angle (μ_s) for fixed snow surface state variables modelled with AART, and fixed atmospheric state variables modelled with libRadtran (viewing geometry was fixed as well). State variables and solar/view geometry were based on a PRISMA acquisition over southern Idaho on 8

December 2022. Figure (B) shows normalized radiance with respect to peak TOA radiance across wavelengths to highlight the change in shape.

However, if we were only to optimize μ_s, the other key terms, local viewer zenith angle (μ_v) and local phase angle (ξ) in the AART formulation for bidirectional reflectance of snow (Eq. 2) (Kokhanovsky & Zege, 2004; Kokhanovsky et al., 2021a) would remain constant from the available DEM (i.e., μ_s, μ_v, ξ are all derived from DEM) ~~(Eq. 2; Wilder et al., 2024)~~,

$$r_{snow}(\mu_s, \mu_v, \xi, \lambda) = r0(\mu_s, \mu_v, \xi)\ \cancel{a_{snow}(\lambda)} a_{snow}(\lambda)^f \qquad (2)$$

where $r0$ is the reflection function of a semi-infinite non-absorbing snow layer (Tedesco & Kokhanovsky, 2007), α_{snow} is the ~~plane~~ spherical albedo [plane albedo can be computed using (26) in Kokhanovsky et al. (2021a)], f is the escape function (Kokhanovsky et al., 2021a), and r_{snow} is the bidirectional reflectance of snow. Keeping other terms μ_v *and* ξ the same are problematic because snow reflectance is poorly approximated as a non-Lambertian surface (Leroux & Fily, 1988), and the outcome will be greatly influenced by μ_v *and* ξ. Therefore, to incorporate solving for $\mu_s, \mu_v,$ *and* ξ from TOA radiance into ~~the~~

~~GOSHAWK~~the algorithm, we instead elect to optimally solve for cos(aspect) (i.e., “northness”) and sin(aspect) (i.e., “eastness”) (Table 1).

Table 1. Parameter space and initial vectors used in numerical optimization for PRISMA data.

Parameter [unit]	**Definition**	**Feasible Range**	**Initial State**	**Type**
f_{snow} [%]	Fractional snow in the mixed pixel	[0, 100]	10	Surface
f_{shade} [%]	Fractional shade in the mixed pixel	[0, 100]	20	Surface
f_{LC1} [%]	Fractional cover of endmember 1 (based on land cover value at pixel)	[0, 100]	50	Surface
f_{LC2} [%]	Fractional cover of endmember 2 (based on land cover value at pixel)	[0, 100]	20	Surface
SSA [m^2 kg^{-1}]	Specific surface area (SSA)	[2, 156]	40	Surface
LAP [µg g^{-1}]	Concentration of light absorbing particles, LAP, modelled as dust (PM-2.5).	[0, 145]	0	Surface
Liquid water [%]	Percentage of liquid water on the snow surface	[0, 50]	2	Surface
AOD 550 [%]	Dimensionless Aerosol Optical Depth (AOD) at 550 nm	[1,100]	10	Atmospheric
H_2O [mm]	Columnar water vapor in the atmosphere	[1,50]	1	Atmospheric
Eastness	sin(aspect)	[-1,1]	Variable	Topographic
Northness	cos(aspect)	[-1,1]	Variable	Topographic

Aspect can be solved during optimization by using the atan2 function.~~ (Van Rossum, 2020).~~ We chose to use this method because eastness and northness are continuously differentiable, and therefore, are suited for numerical optimization methods, whereas aspect is discontinuous at north (using the convention of 0 and 360 degrees as north)~~is circular~~. We then can use this optimal aspect to estimate μ_s (Eq. 1), μ_v~~ (Eq. 3)~~, and ξ~~ (Eq. 4)~~.~~,~~

$$\cancel{\mu_v = \max[0, \cos(\theta_v)\cos(S) + \sin(\theta_v)\sin(S)\cos(\phi_v - A)] \quad (3)}$$

$$\cancel{\xi = \cos^{-1}(-\mu_s\mu_v + sin(\theta_i)\, sin(\theta_v)\, cos(180 - (\phi_v - \phi_0))) \quad (4)}$$

~~where ϕ_v is the viewing azimuth angle, and θ_v is the viewer zenith angle on a flat plane.~~

T~~T~~his directly impacts Eq.2 and Eq. 5 (~~and the~~ formulation of incoming solar energy in the model) (Picard et al., 2020),

$$E(\lambda) = \psi\mu_s E(\lambda)_{dir} + V_\Omega E(\lambda)_{diff} + \left[\left(1 + \frac{\cos(S)}{2} - V_\Omega\right) r(\lambda)_{surf} E(\lambda)_{diff} \cancel{\left(E(\lambda)_{dir} + E(\lambda)_{diff}\right)}\right] \quad (5)$$

where E is total incoming irradiance, ψ is binary shade or no shade, E_{dir} and E_{diff} are the direct and diffuse irradiance, respectively, V_Ω is the sky view factor (Dozier, 2022), and r_{surf}

is the reflectance of nearby terrain (which is assumed to be equal to the pixel itself). ~~Explicitly within GOSHAWK the following equation is then~~The term E is ~~-~~solved ~~using~~ within our non-linear numerical optimization method as described in ~~(~~Wilder et al. (~~,~~2024). This was modelled incorrectly in Wilder et al. (2024); however, this was corrected in this paper where only diffuse irradiance is used in the 3rd term in Eq. 5. Also, ~~-~~a~~A~~dding in the two extra parameters (eastness and northness) in our updated optimization scheme did not change our run time significantly. ~~, which still hovered around 15 minutes (depending on the image), as noted in Wilder et al. (2024). It is~~Caution is advised against solving for slope *and* aspect in the inversion due to the non-unique solution space (Figure 1); however, only considering aspect ensures unique solutions of aspect, μ_s, μ_v, and ξ. We chose aspect because of its greater impact on determining partition of direct and diffuse illumination and has been found to be more impactful to errors associated with snow property retrieval (Donahue et al., 2023). ~~also worth noting that while the optimal aspect cannot be solved accurately due to a non-unique solution space (Figure 1), the resulting~~ $\cancel{\mu_s}$, $\cancel{\mu_v}$ ~~, and~~ $\cancel{\xi}$ ~~are unique and the solution is such.~~ In this study we used estimate of total ozone column as input into creating the libRadtran look up table specific for each image. We used the average weekly ozone over the bounds of the image from Sentinel-5P NRTI O3: Near Real-Time Ozone dataset. This approach serves an improvement over Wilder et al. (2024), where ozone was fixed at 300 Dobson Units.

2.~~2~~ 3 Estimating snow properties from AVIRIS-NG for validation

Due to the fine signal to noise ratio and ~~the higher~~ spatial resolution of AVIRIS-NG, we treated the dataset as the ground reference. It also captured a similar spectral range to PRISMA which made it a suitable comparison dataset. The main assumption here is that AVIRIS-NG pixels at 4 m are relatively homogenous and are either snow or no-snow – which may not always be the case. This could be a potential source of uncertainty in our analysis ~~It also captured a similar spectral range to PRISMA which made it a suitable comparison dataset.~~ . To select snow-covered pixels, we solved for NDSI (Normalized Difference Snow Index) using bands at 600 nm and 1500 nm. We limited our retrieval of snow properties for NDSI greater than or equal to 0.90 (Painter et al., 2013). A common approach to retrieve snow grain size from pure snow pixels is to apply the scaled band area algorithm (Nolin & Dozier, 2000); however, it is recognized that the large presence of ~~LWC~~ liquid water is a limitation. The maximum air temperature of 10.8° C on the day of the image at the San Juan Mountains site indicated that elevated ~~LWC~~ liquid water at the surface was probable (Center for Snow and Avalanche Studies, 2023). Additionally, reflectance spectra appeared to be shifted along the x-axis (wavelength) due to the presence of ~~LWC~~liquid water. Therefore, we used constrained non-linear numerical optimization to model apparent snow reflectance with AART by allowing fractional snow, fractional shade, liquid water~~LWC~~, and

SSA to vary. We did not include rock or forest endmembers in this formulation, assuming the 4 m pixels are relatively homogenous as previously stated. Topographic incident angles were held constant based on the 4 m resolution DEM provided by AVIRIS-NG. We minimized Root Mean Square Error (RMSE) between observed-apparent and modelled-apparent snow reflectance from AART wavelengths in the range, 1000-1250 nm. This range has high ice absorption and limited impacts from atmospheric interference and LAP (Miller et al., 2016). ~~greater than 900 nm and not impacted by atmospheric interference and LAP (Miller et al. 2016) (901-1299 nm, 1451-1779 nm, and 1951-2449 nm).~~ The presence of ~~LWC~~ liquid water was included in our analysis by means of the composite refractive index of water and ice (Donahue et al., 2022; Hale & Querry,1973; Warren & Brandt, 2008). We assumed similar grain shape assumptions for both PRISMA and AVIRIS-NG, and that if there is a bias due to this it should be consistent between the two datasets in our analysis.

2.4 Comparing modelled ~~snow albedo and SSA~~snow properties

The ~~GOSHAWK~~ algorithm was used in two different modes: 1) static topography based on the Copernicus DEM (hereon called "***static***"); and 2) solved topography based on the algorithm updates (hereon called "***radiance***"). To compare the accuracy of PRISMA derived SSA and ~~LWC~~liquid water, we resampled the AVIRIS-NG optical property results (SSA and LWC) to match the PRISMA resolution (30 m) and extents by using bilinear interpolation. Then, we sampled all valid pixels where PRISMA and AVIRIS-NG had snow. We then computed r-pearson correlation coefficient, Mean Bias, and RMSE for the radiance and static methods (with respect to AVIRIS-NG). Finally, we used Copernicus derived slope and aspect maps to determine where the largest errors were occurring on the landscape to compare with the theoretical basis presented in Figure 1. We do this by using the ~~Mean Absolute Error (MAE)~~mean absolute difference with respect to μ_s ~~slope and aspect~~. We expected to see higher differences in north facing aspects (i.e., μ_s approaches 0), and where θ_0 was higher. To test the interaction with θ_0 more fully, we extended the analysis to Mount Shasta, CA, and Toolik, Alaska, where no in *situ data* existed. ~~Finally, we~~We compared the modelled ~~broadband albedo and SSA~~properties between the radiance and static methods to assess how these assumptions ~~propagated into outputs.~~impacted results for these types of data at 30 m scale.

2.5 Comparing DEM and radiance derived μ_s

To ensure the resulting radiance derived μ_s were valid we downloaded the best available validation data sources for comparison. For the San Juan and Shasta sites, we collected DEM products at 1 m spatial ~~resolution and~~resolution and collected 5 m spatial resolution DEM for the Toolik site (U.S. Geological Survey, 2019; U.S. Geological Survey, 2022). Then, we computed slope, aspect, solar zenith angle, and solar azimuth angle for all pixels to compute μ_s at the native resolution (Eq. 1). Then, we used bilinear interpolation to resample the 1 m and 5 m products to 30 m to exactly match the extents and resolution of our PRISMA images. We would like to acknowledge that while these are the best freely available datasets for our images, they still do not capture the true snow-on topography, and instead are a representation of the "snow-free" surface. We compared matching pixels to determine RMSE, R^2, and Mean Bias. Pixels that were marked as shadow from ray tracing were excluded from this comparison.

3 Results

3.1 Validation using AVIRIS-NG data over the San Juan Mountains

~~Over all flightlines~~Over the area of the flightlines, AVIRIS-NG estimated mean SSA = 18.0 +/- 8.3~~13.18~~ $m^2\ kg^{-1}$, PRISMA radiance method estimated mean SSA = ~~23.67~~19.6 +/- 5.8~~12.45~~ $m^2\ kg^{-1}$, and PRISMA static method estimated mean SSA = 22.0~~25.06~~ +/- ~~16.06~~12.1 $m^2\ kg^{-1}$. When comparing the SSA performance over each pixel to the AVIRIS-NG flightlines (Figure 4) we found the PRISMA radiance method (r=0.43; RMSD=8.0 $m^2\ kg^{-1}$; bias=+1.7 $m^2\ kg^{-1}$; n=36,412) performed slightly better than the static method (r=0.23; RMSD=13.6 $m^2\ kg^{-1}$; bias=+4.0 $m^2\ kg^{-1}$; n=36,412) for SSA.

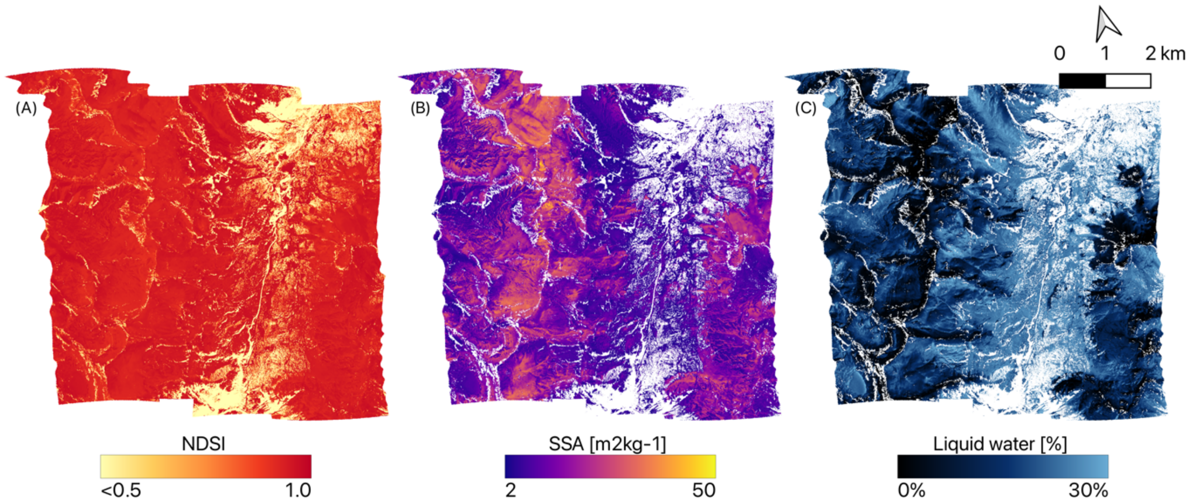

Figure 4. Snow properties computed from AVIRIS-NG (4 m spatial resolution) on 29 April 2021 including NDSI (A), SSA (B), and LWC (C) for the San Juan Mountains site.

There was not a significant improvement in liquid water estimation between radiance (r=0.67; RMSD=10%; bias=-8%; n=36,412) and static (r=0.67; RMSD=10%; bias=-9%; n=36,412). Furthermore, it appeared that there was a consistent liquid water bias of 8 to 9%, hinting that more melt had occurred during the AVIRIS-NG flights. As previously noted, the temperatures were well above freezing during the overpass of AVIRIS-NG and occurred roughly 1 hour later in the day compared to the PRISMA acquisition. This most likely explains the higher ~~LWC~~ liquid water and lower SSA observed by AVIRIS-NG. We further tested this by masking out areas where AVIRIS-NG liquid water content was greater than 0.1%, to establish areas where low amounts of melt occurred between the two acquisitions. We found that performance of

PRISMA static (RMSD=14.2 $m^2\ kg^{-1}$; rRMSD=49%; n=181) and radiance (RMSD=6.9 $m^2\ kg^{-1}$; rRMSD=23%; n=181) methods were more accurate for these areas. The radiance method performed slightly better, suggesting a modest 25% improvement in accuracy for SSA over the static method when considering pixels that were less impacted by melt.

Additionally, comparing all pixels we found improvement from radiance occurred mostly on steep, north facing aspects (e.g., when μ_s approached 0). We found the absolute residual increased as μ_s approached zero for the static method ($r = -0.47$; $p<0.01$), while this relationship was diminished nearly by a factor of 5 for the radiance method ($r = -0.10$; $p<0.01$) (Figure 5.A). These errors were caused by incorrect terrain information in the inversion, where inversion error increased proportionately in the static method (Figure 5.B).

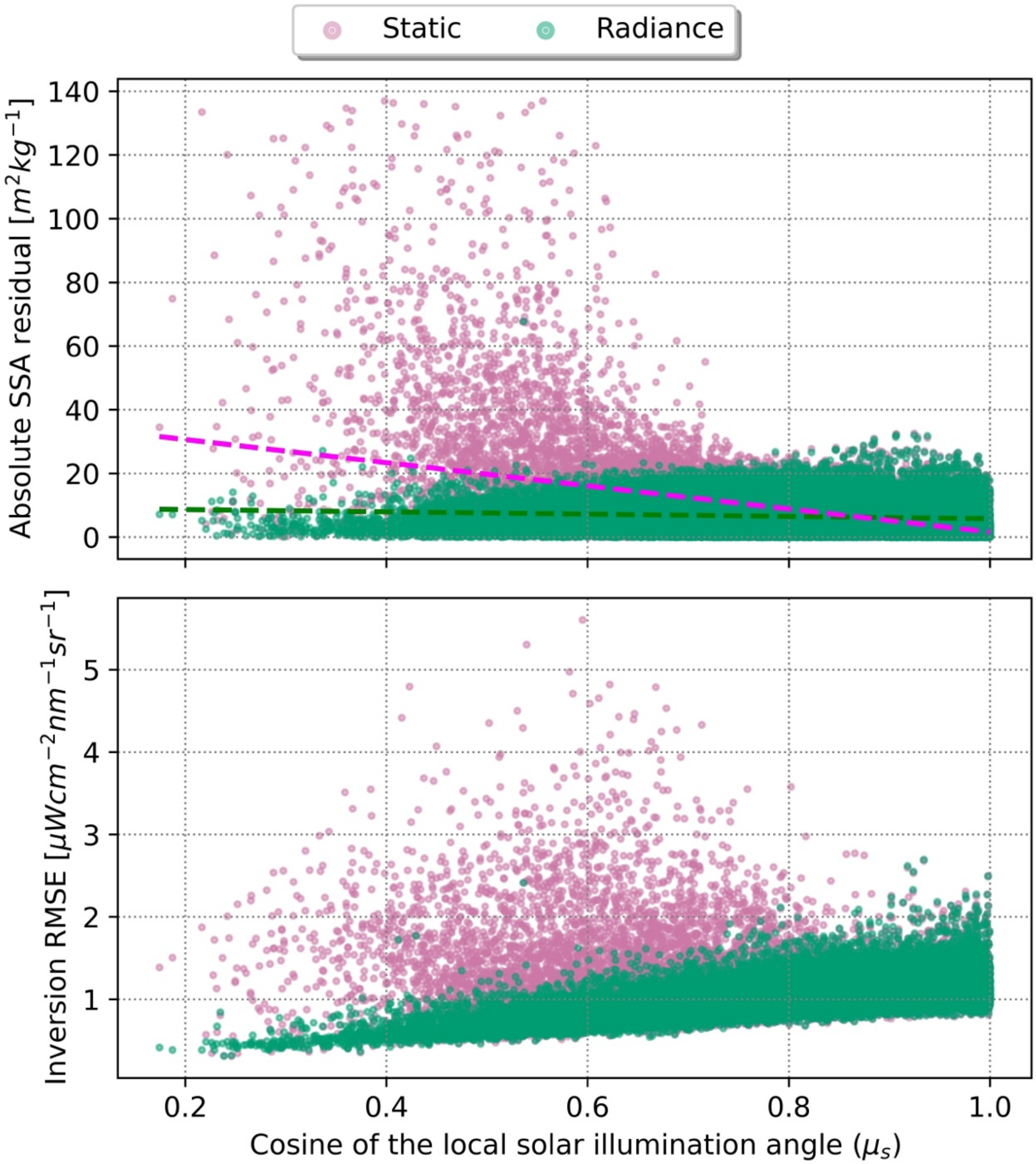

Figure 5. Absolute difference in modelled SSA when compared to AVIRIS-NG for radiance method (green) and static method (pink) respect to μ_s (A) and resulting RMSE from the

inversion from PRISMA with respect to μ_s (B). Error in the static method increases significantly when μ_s approached zero (r = -0.47; p<0.01); however, the difference was less noticeable in the radiance method (r = -0.10; p<0.01).

3.2 Comparing radiance and static methods between sites

On average across each of the images, radiance and static methods provided similar retrieved parameters within less than one standard deviation (Table 2). In general, this means there is not a significant difference at the 30 m scale for computing parameters such as SSA and broadband albedo (BA) when considering the entire image. Interestingly when terrain is fixed, the static model compensated for incorrect illumination by increasing the aerosol optical depth (thereby reducing the amount of direct solar radiation). Investigating the errors more closely, we found much larger differences in retrieved properties where μ_s approached 0 (Figure 6). The difference in distributions matched closely to the theoretical demonstration (Figure 1) and is most likely associated with the standard error of slope and aspect from Copernicus DEM given the illumination conditions. This result also demonstrates the difference between the two methods had the biggest impact for images where θ_0 was high, resulting in potentially inaccurate retrievals that impact both surface and atmospheric state variables on relatively mild slopes.

~~Interestingly when terrain is fixed, the static model compensated for incorrect illumination by increasing the aerosol optical depth (thereby reducing the amount of direct solar radiation).~~). ~~The difference in distributions matched closely to the theoretical demonstration (Figure 1) and is most likely associated with the standard error of slope and aspect from Copernicus DEM given the illumination conditions. This result demonstrated that the difference between the two methods had the biggest impact for images where~~ θ_0 ~~was high.~~ ~~On average for the Mount Shasta site, the radiance method estimated SSA was 17.57 +/- 14.58~~ m^2 kg^{-1}~~, and static method SSA was 17.74 +/- 12.67~~ m^2 kg^{-1} ~~(Table 3). Notably, there were more data gaps in the static method, resulting from failed inversions likely due to errors in the slope and aspect. On average for the Toolik site the radiance method estimated SSA to be 51.50 +/- 12.46~~ m^2 kg^{-1}~~, and the static method estimated 52.07 +/- 14.49~~ m^2 kg^{-1}~~.~~

Table 2. Image-wide statistics comparing derived properties ~~of SSA and broadband albedo~~ between the two methods (static vs. radiance) processing the PRISMA imagery for all three sites.

Site	PRISMA Method	Mean SSA [~~(~~m^2 kg^{-1}]~~)~~	Mean Broadband Albedo~~Standard Deviation of SSA (m^2 kg^{-1})~~	~~Mean Broadband Albedo~~Mean Liquid water [%]	~~Standard Deviation of Broadband Albedo~~Mean AOD at 550 nm	Mean water column vapour [mm]

San Juan	Static	23.3 ~~2.14~~+/- 14.9	0.79 +/- 0.03~~19.40~~	3.5 +/- 4.8~~0.79~~	0.05 +/- 0.13~~0.03~~	6.7 +/- 1.1
	Radiance	19.6 +/- 5.9 ~~21.27~~	0.78 +/- 0.03~~15.94~~	3.9 +/- 5.0~~0.78~~	0.01 +/- 0.01~~0.04~~	6.8 +/- 0.3
Shasta	Static	11.04 +/- 6.03~~17.74~~	0.77~~8~~ +/- 0.04~~12.67~~	1.6 +/- 3.3~~0.74~~	0.04 +/- 0.107~~0.05~~	7.6 +/- 1.3~~0~~
	Radiance	10~~1~~.7~~3~~ +/- 6.26 ~~17.57~~	0.77~~8~~ +/- 0.05~~14.58~~	1.9 +/- 3.8~~0.72~~	0.01 +/- 0.04~~0.06~~	7.7 +/- 1.1~~9~~
Toolik	Static	30.1 +/- 9.6~~52.07~~	0.85 +/- 0.02~~14.49~~	0.0 +/- 0.0~~0.82~~	0.02 +/- 0.03~~0.03~~	1.0 +/- 0.4
	Radiance	27.7 +/- 7.9~~51.50~~	0.84 +/- 0.02~~12.46~~	0.0 +/- 0.0~~0.81~~	0.01 +/- 0.01~~0.03~~	1.0 +/- 0.2

~~When looking more closely at these errors we found6~~

~~Additionally, we saw the highest difference between the two methods on north facing aspects, where μ_s approached 0 (Figure 7). The difference in distributions matched closely to the theoretical demonstration (Figure 1) and is most likely associated with the standard error of~~

~~slope and aspect from Copernicus DEM given the illumination conditions. This result demonstrated that the difference between the two methods had the biggest impact for images where θ_0 was high.~~

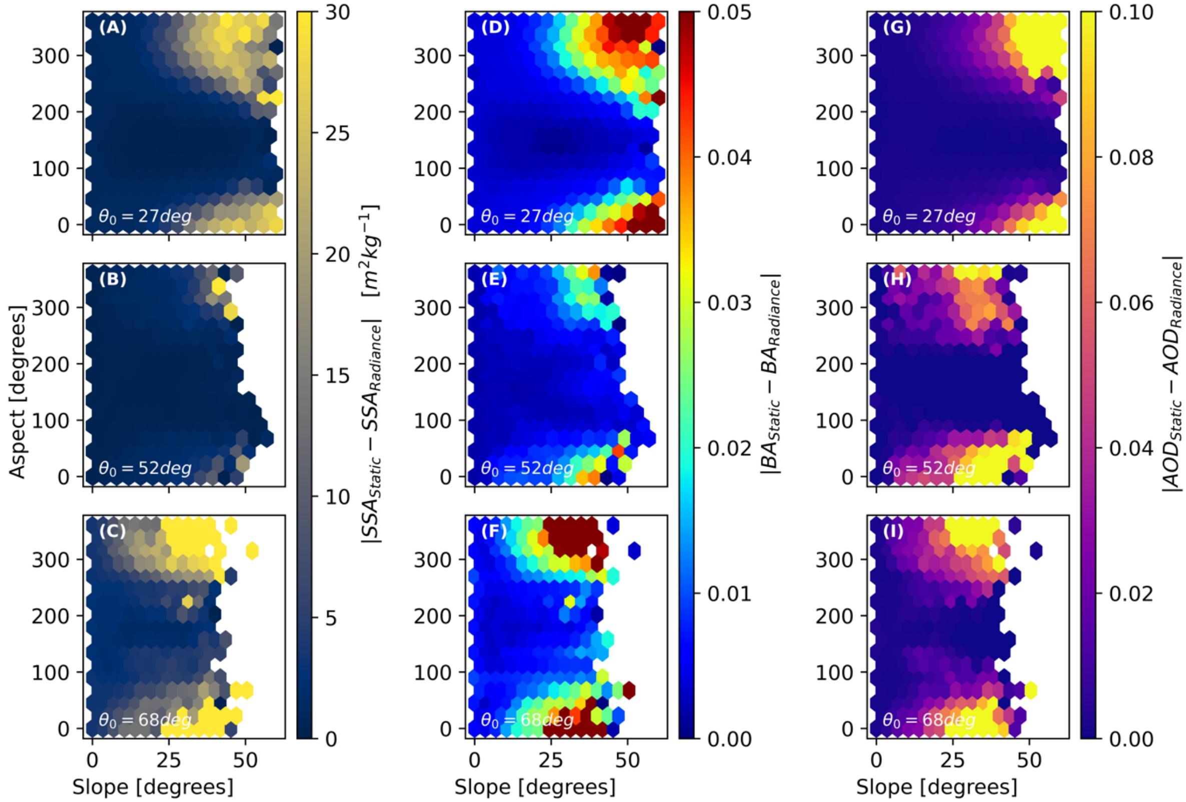

Figure 6. 2D Histogram plots showing absolute ~~error~~ difference in SSA (left), broadband albedo (middle) and AOD (left) with respect to slope and aspect across the entire dataset. In this figure ~~, treating radiance method as validation,~~ absolute difference is calculated as |Static – Radiance|. This is shown for the San Juan Mountains site (A,D,G), Shasta site (B,E,H), and Toolik site (C,F,I). The average solar zenith angle (θ_0) is shown for reference on each panel.

Putting this into spatial context (Figure 7), San Juan site had 37% of pixels (135.3 km^2) with an absolute difference in BA (|δBA|) >= 0.01 and 14% pixels (49.9 km^2) with |δBA| >= 0.02. Shasta site had 30~~28~~% of pixels (16~~4~~.7~~1~~ km^2) with |δBA| >= 0.01 and 9% pixels (5.1 km^2) with |δBA| >= 0.02. Toolik site had 40% of pixels (325.3 km^2) with |δBA| >= 0.01 and 8% pixels (66.6 km^2) with |δBA| >= 0.02.

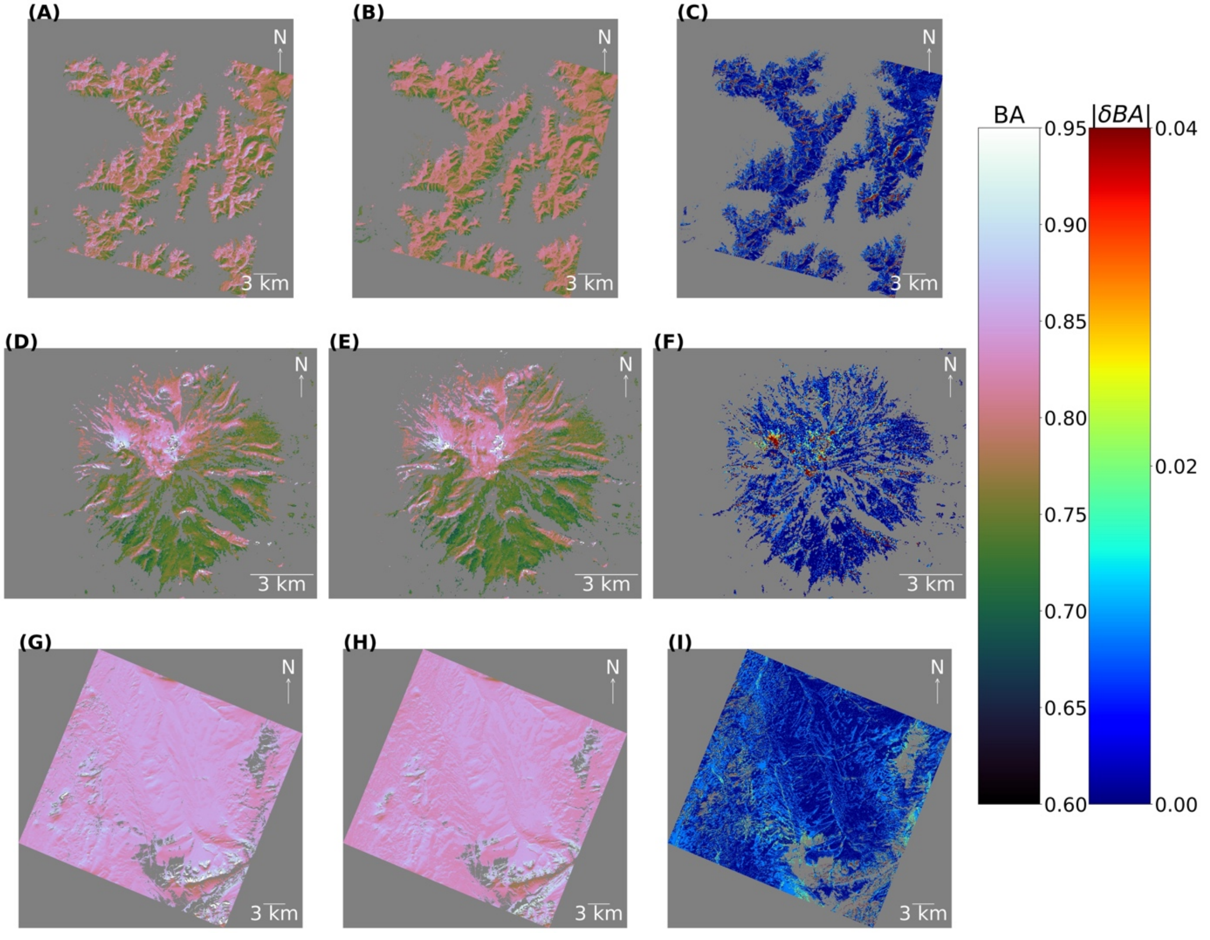

~~We observed a small but notable difference between the methods in derived snow broadband albedo (BA) values (Figure 8). On average the standard deviation between $BA_{Static} - BA_{Radiance}$ (δBA) for the San Juan Mountains site was 0.02, standard deviation for the Shasta site was 0.01, and standard deviation for the Toolik site was 0.02. Generally, there was not a clear bias with respect to μ_s. For the San Juan Mountains site, most of the pixels from the static method showed a consistent small, negative bias of around -0.002. However, for shadier slopes at this site, this bias flipped positive and was much more uncertain at around +0.02. Interestingly, δBA from the Toolik site had the opposite relationship to San Juan Mountains site, where δBA was more positive on sunnier slopes (μ_s approaching 1), and more negative on shadier slopes (μ_s approaching 0), suggesting there could be different mechanisms for which the static method may lead to inaccuracies. The result for the Toolik site confirms the need to model the illumination conditions even in relatively flat terrain, because of implications for net radiative forcing in the cryosphere. The Mount Shasta site δBA had no strong relationship with respect to μ_s~~

Figure 7. Modelled broadband snow albedo (BA) for San Juan Mountains site (A-C), Shasta Mountain site (D-F), and Toolik site (G-I). Left column represents BA from static method, middle column represents BA from radiance method, and right column represents absolute difference in BA (|δBA|). Dark grey colour symbolizes data that is not a value.

Median |δBA| for all sites with respect to $\boldsymbol{\mu_s}$ general increased as $\boldsymbol{\mu_s}$ approached zero (Figure 8). For example, for the San Juan site, ~~-~~median |δBA| ranged from 0.03 to 0.00 across μ_s. For the Shasta and Toolik sites, median |δBA| ranged from 0.02 to 0.00 across μ_s. This relation was ~~highly~~ non-linear and depended on the site and illumination conditions~~. For example, standard deviation of |δBA| (shown as the shaded regions in Figure 9) for well-lit slopes (~~$\boldsymbol{\mu_s} > \mathbf{0.8}$~~) were generally smaller for San Juan site, and conversely were higher for the Toolik site. Similar to Dozier et al. (2022), one can see a monotonic relation with respect to~~ ~~$\boldsymbol{\theta_0}$~~ ~~across the three sites~~. This analysis demonstrates the levels of uncertainty potentially left in for retrievals relying on static, non-coincident DEMs. This shows quantitatively the improvements to snow broadband albedo at 30 m scale by using radiance-based approach to be relatively small for well-lit slopes – on the order 0-1%. While shaded slopes may have errors in snow broadband albedo on the order of 1-3%. Interestingly for the Toolik site, |δBA| also increased as $\boldsymbol{\mu_s}$ approached one.

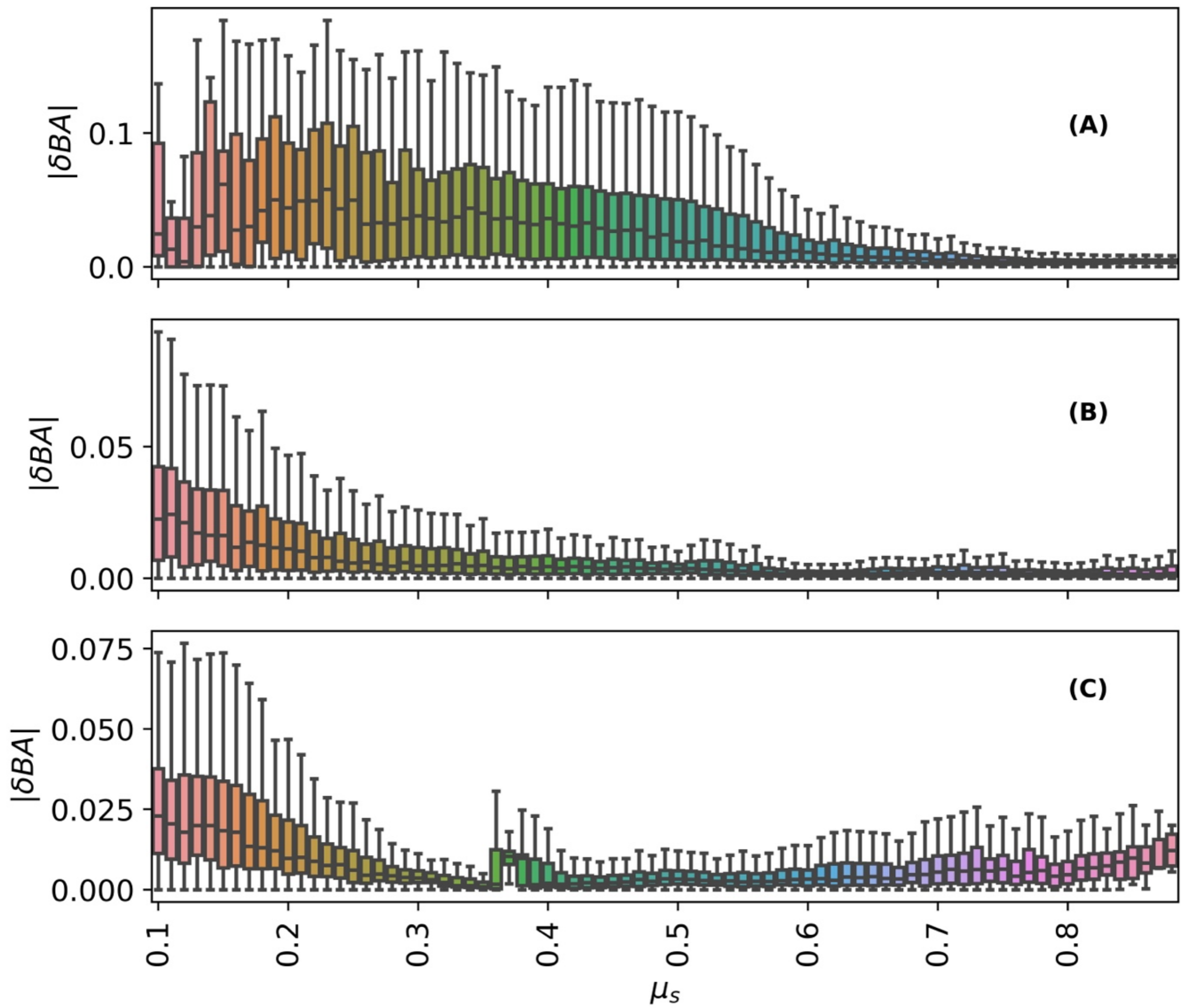

Figure 8. Modelled absolute difference in broadband albedo ($|\delta BA| = |BA_{Static} - BA_{Radiance}|$) for San Juan (A), Shasta (B), and Toolik (C). Note these boxplots were created by rounding μ_s to the nearest hundredth place.

3.3 Comparing DEM and radiance derived μ_s

At the 30 m pixel scale, Copernicus DEM derived μ_s had similar overall performance to radiance derived μ_s (Figure 9), with Copernicus DEM derived μ_s having slightly higher performance. For example, for the San Juan site, RMSD only varied by 0.006 between the two methods. Similarly, the R^2 for Copernicus derived μ_s was 0.86, while the radiance derived μ_s was slightly lower at 0.83. This similar overall performance was common amongst the three sites. We found the average bias for radiance derived μ_s was generally closer to zero (+/- 0.01), and did not show a strong negative or positive direction.

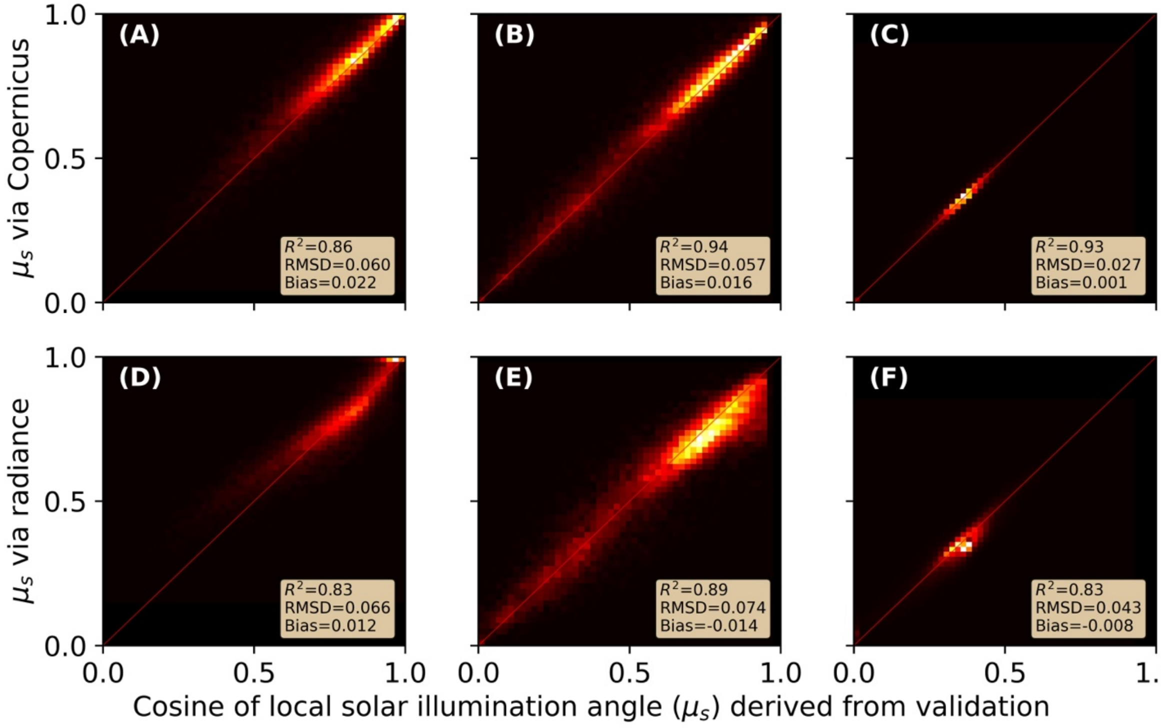

Figure 9. Comparing μ_s at 30 m pixel scale derived from radiance and Copernicus against high resolution DEM for San Juan site (A,D), Shasta site (B,E), and Toolik site (C,F).

4 Discussion

4.1 ~~Implications in accounting for terrain in snow property retrieval~~Radiance derived DEMs may replace coincident DEMs and contain information related to surface roughness

Derivative slope and aspect maps are prone to errors at 30 m spatial resolutions (Dozier et al., 2022).~~,~~ This~~which~~ is~~become~~ relevant for derived snow products from upcoming missions such as SBG and CHIME which will rely on ~~such~~ topographic information to calculate optical properties like snow albedo ~~so that we can better monitor seasonal snowmelt~~. These errors can be inherent to the DEM itself, or a product of spatial and/or temporal misalignments (Carmon et al., 2023). ~~To enable high quality snow products regardless of illumination angles and conditions, we have demonstrated benefits of computing optimal terrain using TOA radiance over snow. This new method is especially useful for steep mountain terrain and/or high latitudes where illumination conditions are suboptimal. The θ_0 (solar zenith angle) was relatively low for the San Juan Mountain site in~~

~~our study, and thus represents a lower bound of the improvement in accuracy one could expect (Figure 1; Dozier et al., 2022). This disparity was demonstrated further for the Mount Shasta and Toolik sites when~~ ~~θ_0~~ ~~was larger (i.e. a greater differences in SSA due to more challenging solar and sensor geometry). Even for the relatively flat Toolik site, we showed that correctly accounting for incidence angels can have an impact when~~ ~~θ_0~~ ~~is large.~~ Our modelled |δBA| with respect to the non-coincident DEM was similar to work by Donahue et al. (2023), who found slightly higher ~~similar~~ uncertainties of ~~δBA~~ broadband albedo (ranging from -10 to 10%) for their investigation on Place Glacier, British Columbia, Canada. With the surface and roughness undergoing dramatic change on glaciers throughout a given season, using this radiance-based approach may be especially impactful for improving estimates over glaciers. ~~We corroborated with this research showing similar ranges of δBA for our three study sites.~~

Snow surface roughness has long been a challenging issue in modelling snow properties from space where the solar incidence angle at high spatial resolution for snow-on DEM is not well known (Bair et al., 2022). Previous research found radiance derived μ_s from airborne imaging spectroscopy showed a negative bias and postulated this could be due to within-pixel topography, shadows, and surface roughness (Carmon et al., 2023). Since a bi-directional reflectance function (BRDF) model was not used in their study, it then would be plausible for the optimal μ_s to compensate for these effects. Interestingly when using a BRDF model in our study (i.e., AART) and solving for aspect optimally (therefore informing μ_s, μ_v, and ξ) we did not find a strong bias – negative or positive. Although, we did not take surface roughness measurements, and therefore do not know to the extent this impacted our study. Within-pixel shadows, textures, and surface roughness remain difficult to validate, and we were unable to achieve this in our study. Future work interested in further understanding this radiance-based approach may investigate how such approaches interact with micro-scale topography through ~~the use of~~ground measurements such as ~~snow-on~~ terrestrial and airborne lidar.

4.2~~2 Future considerations~~Next steps in possibly improving this ~~radiance based~~radiance-based approach

While we solved for a few terrain parameters in this study ~~,~~ we did not entirely remove the use of the DEM ~~the static DEM, even~~ from the radiance method. The elevation from global ~~a~~ DEMs has a much higher confidence than its derivative products (Dozier et al., 2022). Therefore, we used these values to inform our atmospheric routine, as well as our shadow casting ray tracing module ~~in GOSHAWK~~ (Wilder et al., 2024). Additionally, ~~as stated in Wilder et al. (2024), GOSHAWK used the Dozier & Frew (1981)~~ we used the method presented in Dozier (2022) for estimating the sky view factor (V_Ω) based on nearby terrain and the pixel itself. This factor could potentially be problematic but was cited as being not as ~~important~~ impactful as μ_s in propagating error (Dozier et al., 2022). Therefore, we elected to use V_Ω derived from the static Copernicus DEM. However, this could be an area for future improvement, especially in very steep terrain where V_Ω becomes small. It is not advised to attempt to add V_Ω directly into the optimization routine presented in this study, as it is a function of pixel slope and aspect, and therefore, altering V_Ω and aspect together would create invalid solutions.

Finally, we used a static value for slope derived from Copernicus DEM. The slope influences the μ_s term, but also influences the passive radiation from nearby slopes. Ultimately, we concluded that aspect had the largest impact on changing μ_s (Figure 1), as well as large RMSE reported in previous work (Dozier et al., 2022; Donahue et al., 2023), and thus was the focus of our study. Caution is advised in including both slope and aspect together, as non-unique solution space for μ_s may cause the optimization outputs to become invalid. In summary, elevation, V_Ω, and slope remain static in our current implementation. Future work may explore other algorithmic choices to further remove, or improve, static DEM parameters.

Another consideration for improving this method is the inclusion of total column ozone into the optimization. Previous research has been able to use TOA snow reflectance data to retrieve reliable estimates of ozone (Kokhanovsky et al., 2021b). In our paper, we elected for a simpler approach to first investigate the impacts of including terrain in the optimization. In this paper we input a fixed ozone for the entire image based on coincident Sentinel-5 measurements. However, it should be stated that ozone impacts a similar spectral range to μ_s (Figure 10). It therefore may be beneficial to include ozone in the atmospheric lookup-table (e.g., MODTRAN, libRadtran) to enable optimization of ozone as well. This may be beneficial in building more realistic radiance-based methods.

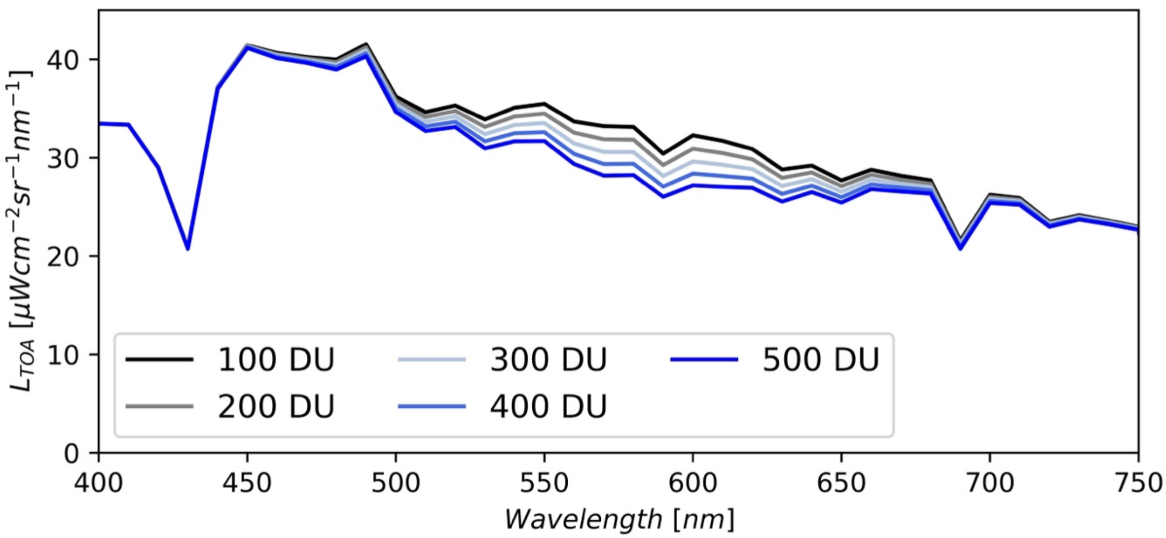

Figure 10. Synthetic data showing change in magnitude of top of atmosphere radiance (L_{TOA}) with respect to changing total column ozone for fixed snow surface state variables modelled with AART, and other fixed atmospheric state variables modelled with libRadtran. Reference data is based on PRISMA image taken over southern Colorado. Note units of total column ozone are shown in in Dobson Units (DU).

Finally, future studies should investigate including improvements to BRDF models of snow (Mei et al., 2022). For example, recent work by Kokhanovsky et al. (2024) has proposed the use of a two-layer model which may be especially useful for vertically heterogenous snowpacks. Their~~is~~ method has been tested using EnMAP data and may easily be transferable to other sensors. The current AART method we used in our paper does not account for these layers, and instead assumes an optically thick, homogenous snowpack. To validate both AART, ~~and~~ the new layered approach, and future BRDF models, snow pit (i.e., vertical profile) measurements of SSA (e.g., Meloche et al., 2023) become essential in ensuring models accurately account for diverse layering of snow ~~(Meloche et al., 2023)~~.

4.3 Big picture implications of the radiance-based approach

This research responds to the objectives stated in "*Thriving on our changing planet: A decadal strategy for Earth observation from space",* to improve biogeophysical modelling at scales driven by topography (National Academies of Science, Engineering, & Medicine, 2018~~9~~), enabling more accurate snow property retrievals in the cryosphere under challenging illumination conditions. Our work presented on solving terrain where DEM data are not available, or reliable, may serve to accelerate improvements to satellite remote sensing tools to monitor and model at both the regional global scale (Sturm et al., 2017), at a critical juncture in time where northern latitudes are changing fast under a warming climate. This includes Earth's glaciers, where radiance-based method may have the largest improvements over static approaches. Our research is complimented by other recent works which show promise in including terrain in the inversions (Bohn et al., 2024; Bohn et al., 2023; Bair et al., 2024; Carmon et al., 2023)

We recommend additional coincident AVIRIS-NG flights with spaceborne imaging spectroscopy datasets to further this work. As we have shown for the San Juan Mountains site, for particularly warm days, images that are separated by longer than an hour may exhibit drastically different SSA and liquid water content. As shown in this paper, this creates an issue when trying to validate improvements to retrieval algorithms.

~~However, future work could investigate other model and optimization configurations to improve upon this study.~~ ~~We recommend additional coincident AVIRIS-NG flights with spaceborne imaging spectroscopy datasets to further this work.~~

5 Conclusion~~s~~

In this study we used existing PRISMA L1 TOA imagery to demonstrate the improvements in modelling snow optical properties when explicitly modelling the terrain in the inversion. This ~~This presents an interesting concept, that end users who are interested in modelling snow from space, are perhaps better off working with the L1 TOA products, and not using the L2 bottom of atmosphere reflectance products space agencies typically produce. This~~ would especially be true for areas where the surface undergoes rapid change, such as ~~on~~ glaciers. This new method is especially useful for steep mountain terrain and/or high latitudes where illumination conditions are suboptimal. The θ_0 (solar zenith angle) was relatively low for the San Juan Mountains site in our study, and thus represents a lower bound of the improvement in accuracy one could expect. This disparity was demonstrated further for the Mount Shasta and Toolik sites when θ_0 was larger (i.e. a greater difference in retrieved properties due to more challenging solar and sensor geometry). Even for the relatively flat Toolik site, we showed that correctly accounting for incidence angles can impact snow properties when θ_0 is large. Future work may look to build from this radiance-based approach to enable better quantification of snow properties at scales impacted by topography.

Code Availability. *https://github.com/cryogars/goshawk*

Author contributions. B.W. created the GOSHAWK algorithm and updates herein, decided on experiment set-up, and performed the subsequent analysis, as well as being the main article writer. J.M., J.E. and N.G. provided ideas, comments, and supervised the work.

Competing interests. The contact author has declared that neither they nor their co-authors have any competing interests.

Acknowledgements. We acknowledge the Italian Space Agency (ASI) for providing us access to PRISMA imagery and providing us the foundational data necessary for this research. We thank Dr. McKenzie Skiles for aiding us in modelling the snow properties from AVIRIS-NG, and for supplying the dataset.

Financial support. This research has been supported by FINESST Award – 21-EARTH21-0249.

References

1. Bair, E. H., Dozier, J., Stern, C., LeWinter, A., Rittger, K., Savagian, A., Stillinger, T., and Davis, R. E.: Divergence of apparent and intrinsic snow albedo over a season

at a sub-alpine site with implications for remote sensing, The Cryosphere, 16, 1765–1778, https://doi.org/10.5194/tc-16-1765-2022, 2022.

2. Bair, E. H., Roberts, D. A., Thompson, D. R., Brodrick, P. G., Wilder, B. A., Bohn, N., Crawford, C. J., Carmon, N., Vuyovich, C. M., & Dozier, J. Brief communication: Not as dirty as they look, flawed airborne and satellite snow spectra. EGUsphere [preprint], https://doi.org/10.5194/egusphere-2024-1681, 2024.

3. Bair, E. H., Stillinger, T., and Dozier, J.: Snow property inversion from remote sensing (SPIReS): A generalized multispectral unmixing approach with examples from MODIS and Landsat 8 OLI, IEEE Transactions on Geoscience and Remote Sensing, 59, 7270–7284, https://doi.org/10.1109/TGRS.2020.3040328, 2021.

4. Bohn, N., Painter, T. H., Thompson, D. R., Carmon, N., Susiluoto, J., Turmon, M. J., and Guanter, L.: Optimal estimation of snow and ice surface parameters from imaging spectroscopy measurements, Remote Sensing of Environment, 264, 112613, https://doi.org/10.1016/j.rse.2021.112613, 2021.

~~4.~~5. Bohn, N., Bair, E. H., Brodrick, P. G., Carmon, N., Green, R. O., Painter, T. H., and Thompson, D. R.: Estimating dust on snow—application of a coupled atmosphere-surface model to spaceborne EMIT imaging spectrometer data, in: IGARSS 2023–

2023 IEEE International Geoscience and Remote Sensing Symposium, 685–688, IEEE, July 2023.

~~5.~~6. Bohn, N., Bair, E. H., Brodrick, P. G., Carmon, N., Green, R. O., Painter, T. H., and Thompson, D. R.: The pitfalls of ignoring topography in snow retrievals: a case study with EMIT, SSRN [preprint], http://dx.doi.org/10.2139/ssrn.4671920, 2024.

~~6.~~7. Carmon, N., Berk, A., Bohn, N., Brodrick, P. G., Dozier, J., Johnson, M., Miller, C. E., Thompson, D. R., Turmon, M., Bachmann, C. M., Green, R. O., Eckert, R., Liggett, E., Nguyen, H., Ochoa, F., Okin, G. S., Samuels, R., Schimel, D., Song, J. J., and Susiluoto, J.: Shape from spectra, Remote Sensing of Environment, 288, 113497, https://doi.org/10.1016/j.rse.2023.113497, 2023.

~~7.~~8. Cawse-Nicholson, K., Townsend, P. A., Schimel, D., Assiri, A. M., Blake, P. L., Buongiorno, M. F., Campbell, P., Carmon, N., Casey, K. A., Correa-Pabón, R. E., Dahlin, K. M., Dashti, H., Dennison, P. E., Dierssen, H., Erickson, A., Fisher, J. B., Frouin, R., Gatebe, C. K., Gholizadeh, H., Gierach, M., Glenn, N. F., Goodman, J. A., Griffith, D. M., Guild, L., Hakkenberg, C. R., Hochberg, E. J., Holmes, T. R. H., Hu, C., Hulley, G., Huemmrich, K. F., Kudela, R. M., Kokaly, R. F., Lee, C. M., Martin, R., Miller, C. E., Moses, W. J., Muller-Karger, F. E., Ortiz, J. D., Otis, D. B., Pahlevan, N., Painter, T. H., Pavlick, R., Poulter, B., Qi, Y., Realmuto, V. J., Roberts, D., Schaepman, M. E., Schneider, F. D., Schwandner, F. M., Serbin, S. P., Shiklomanov, A. N., Stavros, E. N., Thompson, D. R., Torres-Perez, J. L., Turpie, K. R., Tzortziou, M., Ustin, S., Yu, Q., Yusup, Y., Zhang, Q., and SBG Algorithms Working Group: NASA's surface biology and geology designated observable: A perspective on surface imaging algorithms, Remote Sensing of Environment, 257, 112349, https://doi.org/10.1016/j.rse.2021.112349, 2021.

~~8.~~9. Celesti, M., Rast, M., Adams, J., Boccia, V., Gascon, F., Isola, C., and Nieke, J.: The Copernicus Hyperspectral Imaging Mission for the Environment (CHIME): Status and Planning, in: IGARSS 2022–2022 IEEE International Geoscience and Remote Sensing Symposium, 5011–5014, IEEE, July 2022.

~~9.~~10. Center for Snow and Avalanche Studies: Archival Data from Senator Beck Basin Study Area, available at https://snowstudies.org/archived-data/, 2023.

~~10.~~11. Cogliati, S., Sarti, F., Chiarantini, L., Cosi, M., Lorusso, R., Lopinto, E., and Colombo, R.: The PRISMA imaging spectroscopy mission: Overview and first performance analysis, Remote Sensing of Environment, 262, 112499, https://doi.org/10.1016/j.rse.2021.112499, 2021.

~~11.~~12. Dalcin, L., and Fang, Y. L. L.: mpi4py: Status update after 12 years of development, Computing in Science & Engineering, 23(4), 47–54, doi:10.1109/MCSE.2021.3083216, 2021.

~~12.~~13. Donahue, C., Skiles, S. M., and Hammonds, K.: Mapping liquid water content in snow at the millimeter scale: an intercomparison of mixed-phase optical property models using hyperspectral imaging and in situ measurements, The Cryosphere, 16(1), 43–59, https://doi.org/10.5194/tc-16-43-2022, 2022.

~~13.~~14. Donahue, C. P., Menounos, B., Viner, N., Skiles, S. M., Beffort, S., Denouden, T., and Heathfield, D.: Bridging the gap between airborne and spaceborne imaging spectroscopy for mountain glacier surface property retrievals, Remote Sensing of Environment, 299, 113849, https://doi.org/10.1016/j.rse.2023.113849, 2023.

~~14.~~15. Dozier, J.: Revisiting topographic horizons in the era of big data and parallel computing, IEEE Geoscience and Remote Sensing Letters, 19, 1–5, doi:10.1109/LGRS.2021.3125278, 2022.

~~15.~~16. Dozier, J., Bair, E. H., Baskaran, L., Brodrick, P. G., Carmon, N., Kokaly, R. F., and Thompson, D. R.: Error and uncertainty degrade topographic corrections of remotely sensed data, Journal of Geophysical Research: Biogeosciences, 127(11), e2022JG007147, https://doi.org/10.1029/2022JG007147, 2022.

~~16.~~17. European Space Agency: Copernicus Global Digital Elevation Model [Dataset], distributed by Open Topography, https://doi.org/10.5069/G9028PQ, 2021.

~~17.~~18. Green, R. O., Brodrick, P. G., Chapman, J. W., Eastwood, M., Geier, S., Helmlinger, M., and Thorpe, A. K.: AVIRIS-NG L2 Surface Reflectance, Facility Instrument Collection, V1, ORNL DAAC, Oak Ridge, Tennessee, USA, 2023.

~~18.~~19. Guanter, L., Kaufmann, H., Segl, K., Foerster, S., Rogass, C., Chabrillat, S., Kuester, T., Hollstein, A., Rossner, G., Chlebek, C., Straif, C., Fischer, S., Schrader, S., Storch, T., Heiden, U., Mueller, A., Bachmann, M., Mühle, H., Müller, R., Habermeyer, M., Ohndorf, A., Hill, J., Buddenbaum, H., Hostert, P., van der Linden, S., Leitão, P. J., Rabe, A., Doerffer, R., Krasemann, H., Xi, H., Mauser, W., Hank, T., Locherer, M., Rast, M., Staenz, K., and Sang, B.: The EnMAP spaceborne imaging spectroscopy mission for earth observation, Remote Sensing, 7(7), 8830–8857, https://doi.org/10.3390/rs70708830, 2015.

~~19.~~20. Hale, G. M. and Querry, M. R.: Optical constants of water in the 200-nm to 200-µm wavelength region, Applied Optics, 12, 555–563, https://doi.org/10.1364/AO.12.000555, 1973.

~~20.~~21. Kaspari, S., Skiles, M., Delaney, I., Dixon, D., and Painter, T. H.: Accelerated glacier melt on Snow Dome, Mount Olympus, Washington, USA, due to deposition of black carbon and mineral dust from wildfire, Journal of Geophysical Research: Atmospheres, 120(7), 2793–2807, https://doi.org/10.1002/2014JD022676, 2015.

~~21.~~22. Kokhanovsky, A. A., and Zege, E. P.: Scattering optics of snow, Applied Optics, 43(7), 1589–1602, doi:10.1364/AO.43.001589, 2004.

~~22.~~23. Kokhanovsky, A. A.: The Broadband Albedo of Snow, Frontiers in Environmental Science, 9, 757575, https://doi.org/10.3389/fenvs.2021.757575, 2021.

24. Kokhanovsky, A., Di Mauro, B., Garzonio, R., and Colombo, R.: Retrieval of dust properties from spectral snow reflectance measurements, Frontiers in Environmental Science, 9, 644551, https://doi.org/10.3389/fenvs.2021.644551, 2021a.

~~23.~~25. Kokhanovsky, A., Gascoin, S., Arnaud, L., and Picard, G.: Retrieval of snow albedo and total ozone column from single-view MSI/S-2 spectral reflectance measurements over Antarctica, Remote Sensing, 13(21), 4404, https://doi.org/10.3390/rs13214404, 2021b.

~~24.~~26. Kokhanovsky, A., Brell, M., Segl, K., Efremenko, D., Petkov, B., Bianchini, G., Stone, R., and Chabrillat, S.: The two-layered radiative transfer model for snow reflectance and its application to remote sensing of the Antarctic snow surface from space, Frontiers in Environmental Science, 12, 1416597, https://doi.org/10.3389/fenvs.2024.1416597, 2024.

~~25.~~27. Leroux, C., and Fily, M.: Modeling the effect of sastrugi on snow reflectance, Journal of Geophysical Research: Planets, 103(E11), 25779–25788, https://doi.org/10.1029/98JE00558, 1998.

~~26.~~28. Malmros, J. K., Mernild, S. H., Wilson, R., Tagesson, T., and Fensholt, R.: Snow cover and snow albedo changes in the central Andes of Chile and Argentina from daily MODIS observations (2000–2016), Remote Sensing of Environment, 209, 240–252, https://doi.org/10.1016/j.rse.2018.02.072, 2018.

~~27.~~29. Mayer, B., and Kylling, A.: The libRadtran software package for radiative transfer calculations-description and examples of use, Atmospheric Chemistry and Physics, 5(7), 1855–1877, https://doi.org/10.5194/acp-5-1855-2005, 2005.

~~28.~~30. McKenzie, D.: Mountains in the Greenhouse: Climate Change and the Mountains of the Western U.S.A., 10.1007/978-3-030-42432-9, 2020.

~~29.~~31. Mei, L., Rozanov, V., Jiao, Z., and Burrows, J. P.: A new snow bidirectional reflectance distribution function model in spectral regions from UV to SWIR: Model development and application to ground-based, aircraft and satellite observations, ISPRS Journal of Photogrammetry and Remote Sensing, 188, 269–285, https://doi.org/10.1016/j.isprsjprs.2022.04.010, 2022.

~~30.~~32. Meloche, J., Lemmetyinen, J., Meyer, K., Alabi, I., Vuyovich, C. M., Stuefer, S., Marshall, H., Durand, M., and Langlois, A.: SnowEx23 Laser Snow Microstructure Specific Surface Area Data, Version 1 [Data Set], NASA National Snow and Ice Data Center Distributed Active Archive Center, Boulder, Colorado, USA, https://doi.org/10.5067/BSEP59ADC6XN, accessed 16 August 2024.

~~31.~~33. Miller, S. D., Wang, F., Burgess, A. B., Skiles, S. M., Rogers, M., and Painter, T. H.: Satellite-based estimation of temporally resolved dust radiative forcing in snow cover, Journal of Hydrometeorology, 17(7), 1999–2011, https://doi.org/10.1175/JHM-D-15-0150.1, 2016.

~~32.~~34. National Academies of Sciences, Engineering, and Medicine: Thriving on Our Changing Planet: A Decadal Strategy for Earth Observation from Space, National Academies Press, Washington, DC, 716 pp., doi:10.17226/24938, 2018.

~~33.~~35. O'Neel, S., Wilder, B., Keskinen, Z., Zikan, K. H., Enterkine, J., Filiano, D. L., Meehan, T., LeWinter, A., Deeb, E. J., Marshall, H.-P., & Adebisi, N.: Helicopter-

Borne Lidar to Resolve Snowpack Variability in Southwest Idaho, in: AGU Fall Meeting Abstracts, Vol. 2022, C35E-0922, December 2022.

36. Painter, T. H., Seidel, F. C., Bryant, A. C., Skiles, S. M., and Rittger, K.: Imaging spectroscopy of albedo and radiative forcing by light-absorbing impurities in mountain snow, Journal of Geophysical Research: Atmospheres, 118(17), 9511–9523, https://doi.org/10.1002/jgrd.50520, 2013.

~~34.~~ Picard, G., Dumont, M., Lamare, M., Tuzet, F., Larue, F., Pirazzini, R., and Arnaud, L.: Spectral albedo measurements over snow-covered slopes: theory and slope effect corrections, The Cryosphere, 14, 1497–1517, https://doi.org/10.5194/tc-14-1497-2020, 2020.

37.

~~35.~~38. Seidel, F. C., Rittger, K., Skiles, S. M., Molotch, N. P., and Painter, T. H.: Case study of spatial and temporal variability of snow cover, grain size, albedo and radiative forcing in the Sierra Nevada and Rocky Mountain snowpack derived from imaging spectroscopy, The Cryosphere, 10(3), 1229–1244, https://doi.org/10.5194/tc-10-1229-2016, 2016.

~~36.~~39. Siirila-Woodburn, E. R., Rhoades, A. M., Hatchett, B. J., Huning, L. S., Szinai, J., Tague, C., Nico, P. S., Feldman, D. R., Jones, A. D., Collins, W. D., & Kaatz, L.: A low-to-no snow future and its impacts on water resources in the western United States, *Nature Reviews Earth & Environment*, 2(11), 800-819, https://doi.org/10.1038/s43017-021-00219-y , 2021.

~~37.~~40. Skiles, S. M., & Painter, T.: Daily evolution in dust and black carbon content, snow grain size, and snow albedo during snowmelt, Rocky Mountains, Colorado, *Journal of Glaciology*, 63(237), 118-132, doi:10.1017/jog.2016.125, 2017.

~~38.~~41. Skiles, M. and Vuyovich, C. M.: SnowEx21 Senator Beck Basin and Grand Mesa, CO AVIRIS-NG Surface Spectral Reflectance, Version 1 [Data Set], NASA National Snow and Ice Data Center Distributed Active Archive Center, Boulder, Colorado USA, https://doi.org/10.5067/ZAI3M64WWN5V, Date Accessed 02-09-2024.

~~39.~~42. Sturm, M., Goldstein, M. A., and Parr, C.: Water and life from snow: A trillion dollar science question, Water Resources Research, 53(5), 3534-3544, https://doi.org/10.1002/2017WR020840, 2017.

~~40.~~43. Tedesco, M., and Kokhanovsky, A. A.: The semi-analytical snow retrieval algorithm and its application to MODIS data, Remote Sensing of Environment, 111(2-3), 228-241, https://doi.org/10.1016/j.rse.2007.02.036, 2007.

~~41.~~44. U.S. Geological Survey: 3D Elevation Program 1-Meter Resolution Digital Elevation Model (published 20200606), accessed June 1, 2023, at https://www.usgs.gov/the-national-map-data-delivery, 2019.

~~42.~~45. U.S. Geological Survey, 2022, 5 Meter Alaska Digital Elevation Models (DEMs) - USGS National Map 3DEP Downloadable Data Collection, accessed June 1, 2023, at https://www.usgs.gov/the-national-map-data-delivery, 2022.

~~43.~~46. Wang, W., Yang, K., Zhao, L., Zheng, Z., Lu, H., Mamtimin, A., Ding, B., Li, X., Zhao, L., Li, H., Che, T., & Moore, J. C. Characterizing surface albedo of shallow fresh snow and its importance for snow ablation on the interior of the Tibetan Plateau, Journal of Hydrometeorology, 21(4), 815-827, https://doi.org/10.1175/JHM-D-19-0193.1, 2020.

~~44.~~47. Warren, S. G., & Brandt, R. E. Optical constants of ice from the ultraviolet to the microwave: A revised compilation, Journal of Geophysical Research: Atmospheres, 113(D14), https://doi.org/10.1029/2007JD009744, 2008.

~~45. Wilder, B. A., Glenn, N. F., Lee, C. M., Marshall, H. P., Brandt, J., Kinoshita, A. M., ... & Enterkine, J. (2023, July). Global Optical Snow properties via High-speed Algorithm With K-means clustering (GOSHAWK). In *IGARSS 2023-2023 IEEE International Geoscience and Remote Sensing Symposium*(pp. 118-120). IEEE.~~

~~46.~~48. Wilder, B. A., Lee, C. M., Chlus, A., Marshall, H. P., Brandt, J., Kinoshita, A. M., Enterkine, J., Van Der Weide, T., & Glenn, N. F. Computationally Efficient Retrieval of Snow Surface Properties From Spaceborne Imaging Spectroscopy Measurements Through Dimensionality Reduction Using k-Means Spectral Clustering, IEEE Journal of Selected Topics in Applied Earth Observations and Remote Sensing, vol. 17, pp. 8594-8605, doi:10.1109/JSTARS.2024.3386834, 2024.